Microstructure and Mechanical Properties of AISI 316L Produced by Directed Energy Deposition-Based Additive Manufacturing: A Review

applied sciences

MDPI

Review

Microstructure and Mechanical Properties of AISI 316L Produced by Directed Energy Deposition-Based Additive Manufacturing: A Review

Abdollah Saboori *, Alberta Aversa, Giulio Marchese, Sara Biamino, Mariangela Lombardi and Paolo Fino

Department of Applied Science and Technology, Politecnico Di Torino, Corso Duca degli Abruzzi 24, 10129 Torino, Italy; alberta.aversa@polito.it (A.A.); giulio.marchese@polito.it (G.M.); sara.biamino@polito.it (S.B.); Mariangela.lombardi@polito.it (M.L.); paolo.fino@polito.it (P.F.)

* Correspondence: abdollah.saboori@polito.it; Tel.: +39-0110904763

Received: 20 April 2020; Accepted: 6 May 2020; Published: 9 May 2020

Abstract: Directed energy deposition (DED) as a metal additive manufacturing technology can be used to produce or repair complex shape parts in a layer-wise process using powder or wire. Thanks to its advantages in the fabrication of net-shape and functionally graded components, DED could attract significant interest in the production of high-value parts for different engineering applications. Nevertheless, the industrialization of this technology remains challenging, mainly because of the lack of knowledge regarding the microstructure and mechanical characteristics of as-built parts, as well as the trustworthiness/durability of engineering parts produced by the DED process. Hence, this paper reviews the published data about the microstructure and mechanical performance of DED AISI 316L stainless steel. The data show that building conditions play key roles in the determination of the microstructure and mechanical characteristics of the final components produced via DED. Moreover, this review article sheds light on the major advancements and challenges in the production of AISI 316L parts by the DED process. In addition, it is found that in spite of different investigations carried out on the optimization of process parameters, further research efforts into the production of AISI 316L components via DED technology is required.

Keywords: additive manufacturing; directed energy deposition; AISI 316L; microstructure; mechanical properties

1. Introduction

In recent decades, additive manufacturing (AM) technologies, also recognized as three dimensional (3D) printing, has attracted significant attention in different industries [1,2]. In principle, in all-metal AM processes, at first, a solid model is sliced in multiple layers to generate a tool path for the printing machine. Thereafter, the 3D component is produced in a layer-wise process according to the sliced model data. In addition to the sliced model, two main elements are required to build a part: a feedstock material (metal powder or wire) and a heat source, which can be a laser, electron beam or electric arc [3]. In general, AM systems are categorized into two different classes: powder bed systems and powder/wire feed systems [4,5]. In powder bed systems, a layer of powder is spread on the building platform or on the previously solidified layer and is selectively fused via an energy source that can be either electron beam or laser beam [6–8]. The ability to produce high-resolution features and internal channels, as well as precision dimensional control, are considered the main advantages of powder bed AM processes [5,9,10]. In contrast, in powder/wire feed systems, the material is fed directly inside a melt pool which is already formed by a focalized heat source on the

substrate or on the already deposited layer. Directed energy deposition (DED), as a material feed process, uses a focalized heat source, that can be a laser or an electron beam, and a material which can be powder or wire while being delivered directly into the melt pool. It should also be highlighted that in the literature different names are generally reported for this process [11]. A summary of these names is listed in Table 1.

Table 1. Different commercialized names of the directed energy deposition (DED) process.

Acronym	Technology	Ref.
LENS	Laser Energy Net Shaping	[12,13]
LMD	Laser Metal Deposition	[14,15]
LC	Laser Cladding	[16,17]
DMD	Direct Metal Deposition	[18,19]
LAMP	Laser aided manufacturing process	[3,20]
DLF	Direct Laser Fabrication	[21,22]
LPF	Laser Powder Fusion	[23]

In the DED process the deposition pattern is defined by the relative motion between the substrate and the deposition head. This motion can be obtained by moving only the deposition head, only the substrate, or both substrate and deposition head. The method used mainly depends on the size and the geometry of the substrate [24].

In particular, in the laser-powder DED process, which is known as the most versatile DED process, the powder feeding can be implemented by means of either a single nozzle, coaxial nozzle, or multi-nozzle configuration. The laser-powder DED process has gained considerable interest in recent years thanks to the possibility of repairing parts and production of functionally graded materials (FGM) by varying the alloying element content [25]. In addition to the abovementioned merits of this technology, by using the laser-powder DED process it would be also possible to design specific alloys through the in situ alloying process. In fact, it is possible to deliver various powders into the melt pool simultaneously and, as a consequence, achieve a new composition after solidification. Moreover, a high deposition rate, as well as a rather wide process window, make this process very promising, with respect to the other AM processes, to be employed for the production of large components. These flexibilities of the DED process in the production of net-shape parts and repair of high-value components have broadened its application in various sectors such as aerospace, transportation, medical, and defense.

Despite the aforementioned merits, the DED process has a low powder efficiency and final rough surface that should be machined after the building process. Furthermore, previous works have shown that the thermal history of a part produced via the DED process has a marked effect on the microstructure and mechanical performance of components [26–28]. Therefore, the quality of DED parts is mainly defined by the building parameters used during the process. It is well-known that a large number of parameters can be varied in DED, and these include laser power, scan speed, powder feed rate, building atmosphere, deposition pattern, and many others.

In recent years, stainless steels have been intensively processed by AM technologies, mainly owing to the high mechanical properties that make them suitable for a wide range of applications in various industries such as the automotive, aerospace and petrochemical sectors [4,29,30]. AISI 316L steel is by far the most processed and studied, and its success is mainly related to its weldability, corrosion resistance, and tensile properties. Among the AM technologies, the DED process, which can provide a high grade of flexibility in the design and production of large AISI 316L components, could attract significant attention. In fact, large complex parts can be produced via the DED process with a reduction in the weight, the waste of expensive starting material, and the number of costly post-machining steps.

In recent years, a growing body of literature has emerged in which the correlation among process parameters, microstructure, and mechanical properties of DED AISI 316L stainless steel (Figure 1) has been studied [31–35]. For instance, Yadollahi et al. studied the influence of the time interval

between the deposition of layers and the mechanical properties of DED AISI 316L [36]. Saboori et al. investigated the effect of powder recycling and deposition pattern on the microstructure and mechanical properties of AISI 316L samples produced by the DED process [37,38]. Zheng et al. evaluated the effect of DED process parameters on the evolution of the dimensional and surface quality, microstructure, internal surface, and mechanical performance of AISI 316L samples [39]. Terrassa et al. studied the role of hatch rotation angle on the built quality of DED AISI 316L samples [40]. Tan et al. examined the correlation between the porosity, density, and microstructure of AISI 316L samples produced via DED technology [41]. However, it should be highlighted that according to the existing body of literature on the processing of AISI 316L stainless steel via the DED process, microstructure and mechanical properties analyses are the dominant features that have been considered in the previous research (Figure 2). Hence, this paper provides an overview of the microstructure and properties of DED AISI 316L, and summarizes the main effects of the building parameters on the quality of the final products. In fact, the aim of this article is to review the additive manufacturing of AISI 316L alloy by DED in terms of microstructural development and mechanical properties of the samples produced with the optimal process parameters. First, the role of various factors, such as thermal history and process parameters, on the microstructure of DED AISI 316L is reviewed, and thereafter, the influence of different parameters, such as building direction, building parameters, and powder quality, on the mechanical properties of manufactured components is discussed. In general, the target here is not to assemble all of the existing literature about DED of AISI 316L alloy, but to clarify the importance and opportunities of this innovative process in this field.

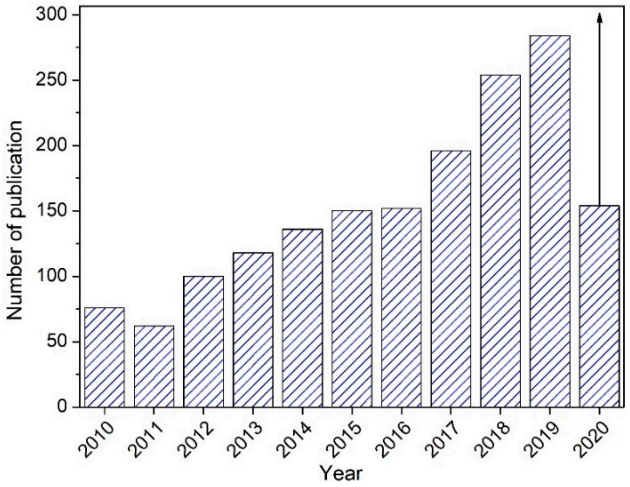

Figure 1. Publication trend in DED AISI 316L chronology between 2010 and 2020 in ScienceDirect (This graph is plotted according to a simple search of "316L" + "DED" at www.sciencedirect.com).

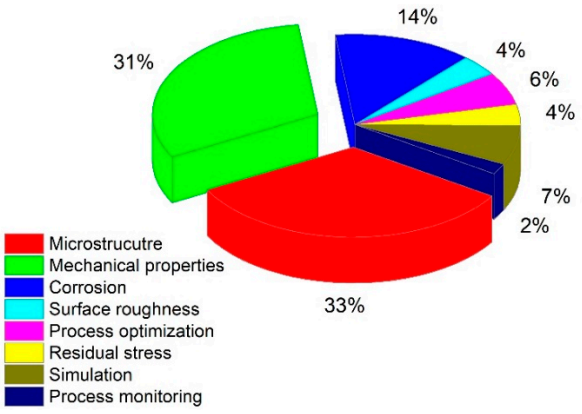

Figure 2. Pie chart showing the percentage of publications at www.sciencedirect.com on different features of the processing of AISI 316L via the DED process.

2. Microstructure

As a thermal process, DED includes a sequence of physical phenomena, such as rapid heating, melting, potential vaporization, and rapid cooling [39]. However, to date, the stability of the microstructure of components produced via DED, which takes place under non-equilibrium conditions, is poorly understood.

In general, the thermal history of DED components, such as the high heating/cooling rate, marked temperature gradient, and bulk temperature increment, define the morphology and grain size of DED components. However, since all of the process parameters and variables have a significant influence on the thermal history of parts, the prediction of microstructural characteristics and their dependence degree remains a significant challenge for metallic materials processed by DED. Nevertheless, to have an effective control mechanism to produce metallic components via DED with excellent mechanical characteristics, it is necessary to overcome this challenge. Therefore, in the literature, several authors have studied the role of specific parameters on the microstructural features and mechanical properties of metallic components produced via DED [4,42–44].

Local solidification rates, the temperature gradient at the liquid/solid interface (G), and the ratio of cooling rate/thermal gradient (R) are the effective parameters that define the final solidified microstructure. In fact, G/R and G × R are found to be the most critical solidification parameters that have a marked influence on the shape of the liquid/solid interface and on the size of microstructure, respectively [45,46]. Substantially, after solidification of metallic parts produced by DED, columnar grains, which represent an elongated morphology that grows in the direction of a maximum thermal gradient, columnar-equiaxed grains, and equiaxed grains are the three structure morphologies that can be formed as a consequence of various G and R values [23]. For instance, it has been revealed that higher solidification rates promote a transition from columnar gain morphology to an equiaxed morphology, and an increment in the cooling rate results in microstructure refinement [27]. Moreover, it should be noted that G/R plays a vital role in the final microstructural morphology, in which low G/R values result in equiaxed structures and high G/R values in columnar structures (Figure 3) [45]. In general, it is found that with cooling rates of 10^3 to 10^4 K/s, it would be possible to achieve desired microstructure and mechanical properties in components produced via DED [23,47]. Part geometry, environmental conditions, and material characteristics are the main factors that can have a marked influence on the optimal G and R values [45].

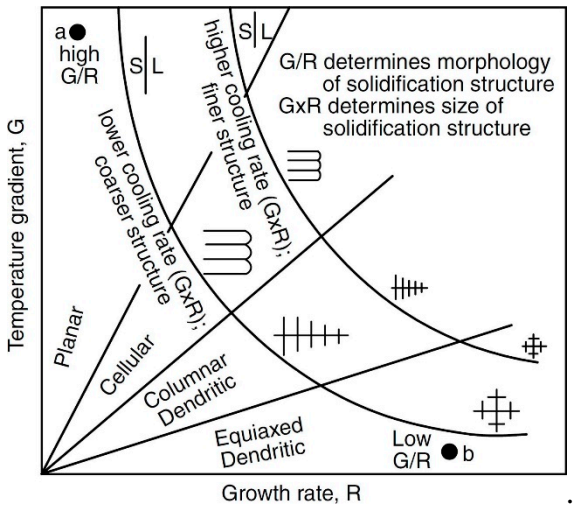

Figure 3. Solidification map showing the effect of temperature gradient and growth rate on the morphology and size of the resulting microstructure [48].

To date, several research studies have been carried out to determine the most effective type of heat transfer mechanism and, consequently, the cooling rate within the AISI 316L components produced by DED [37,49]. As an example, Saboori et al. showed that in an AISI 316L sample different heat transfer mechanisms dominate in different zones of a melt pool with the formation of various

microstructural features [37]. In the central part of the melt pool, where the liquid metal solidifies slightly later, the convective heat transfer mode dominates, whereas at the melt pool borders and across the heat affected zone (HAZ), the solid conduction heat transfer mode is the effective heat transfer mode. In addition, it is reported that at the edges of the laser track, where the lateral sides of the melt pool are exposed to the environment, a complex mix of convective–conductive–radiating heat transfer occurs. Figure 4 reports the general microscopic images of the representative microstructures of as-built AISI 316L samples produced via DED. The first visible feature is the curved border of melt pools, which is the typical AM microstructural characteristic as a consequence of the Gaussian distribution of laser energy (Figure 4a). It is also clear that the temperature gradients in the direction perpendicular to the curved melt pool borders are intense and accordingly lead to the formation of a marked directional growth of the dendrites from the melt pool borders and converging towards the center of the melt pool (Figure 4b). On the contrary, at the central part of the melt pool, owing to the change of heat transfer mode, equiaxed dendrites are more likely to form. Regarding the whole section of the deposited component, as a consequence of the complex heat transfer during the DED process of this alloy, it is found that the columnar structure growing in the direction of the maximum thermal gradient dominates in the middle height of the sample, whereas in the last deposited layers the cellular structure is present [37]. This variation in the microstructure of components along the building direction results in the oscillation in the microhardness values along the building direction. The microhardness of the material decreases at the beginning from the first deposited layer to the second, and thereafter increases gradually toward the last layers [50,51]. This variation in the microhardness of components is found to result from the different velocity of solidification in the sample. In addition, during the deposition, owing to the reheating of previously deposited layers, the middle area is also exposed to cycle reheating that results in the formation of a HAZ area which remains at higher temperatures for a longer period of time. Thus, finer microstructure and higher microhardness are expected for the bottom and top of the DED components which undergo higher cooling rates with respect to other areas. However, the research found a negligible porosity in the final microstructure, even after the optimization of the process parameters.

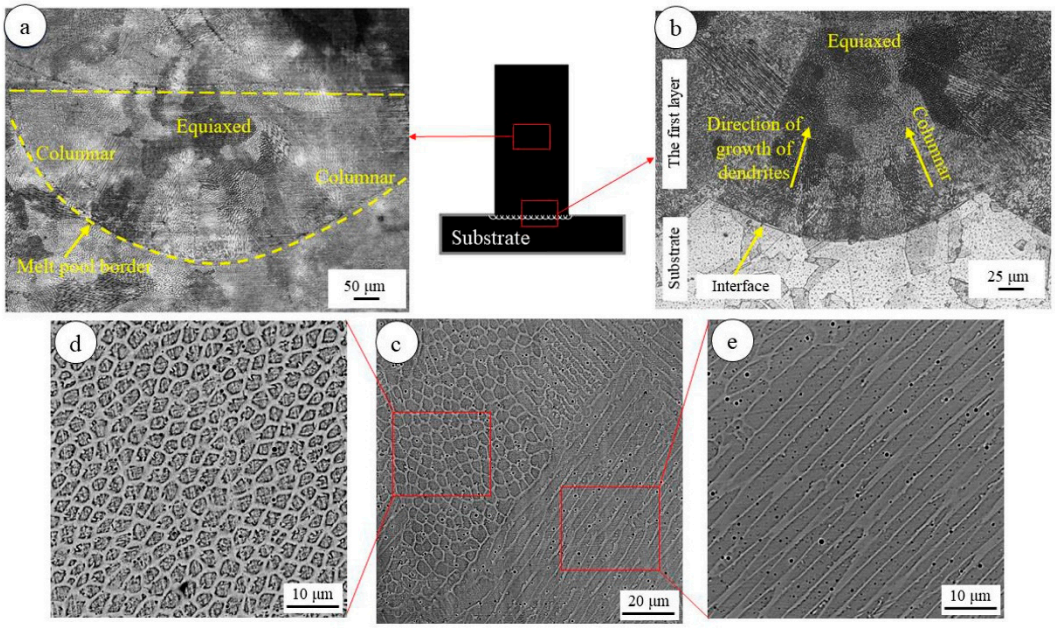

Figure 4. Light optical microscopy micrographs of the DED AISI 316L steel samples produced by DED: (**a**) a representative melt pool at the middle height, (**b**) the microstructure of the first layer, (**c**) SEM images of the columnar and equiaxed microstructures referring to the last deposited layer, (**d**,**e**) high magnifications of (**c**) from two different regions [37].

In another work, Bi et al. studied the microstructure of AISI 316L thin walls produced via DED (Figure 5) [52]. In addition to the typical microstructural characteristics that can be formed in the DED samples, they also reported that the remelting and tempering of the middle layers during the deposition of the next layer, with the exception of the previous layer, are the source of microstructural variations [52].

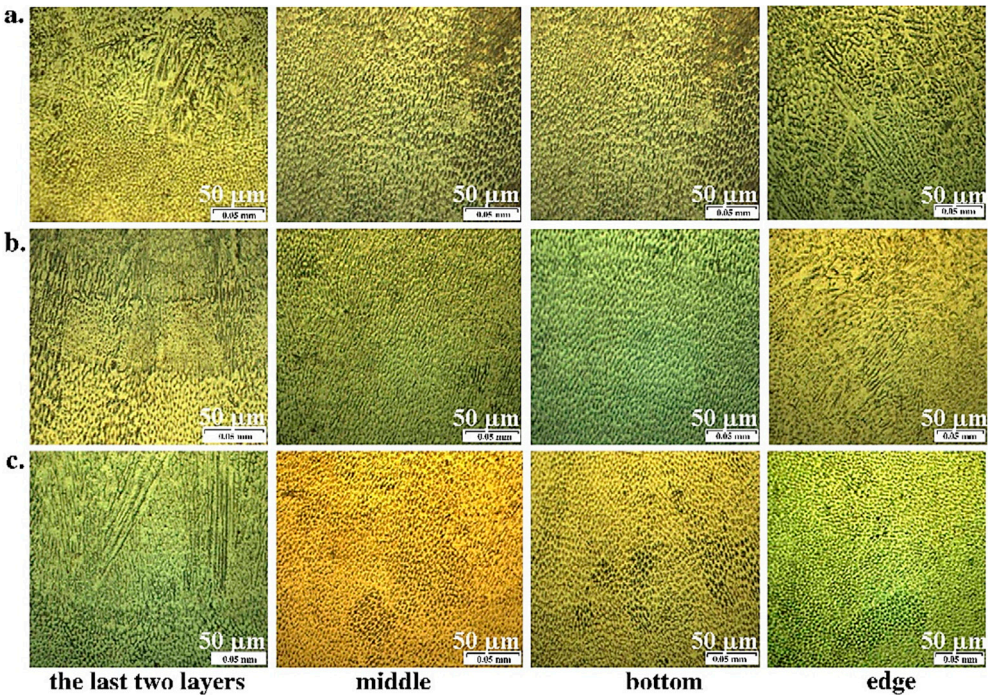

Figure 5. The microstructure of the DED thin walls examined at cross-section and longitudinal section in the middle of the thin wall. a) With a constant laser power of 300 W, b) Process control with a constant set-value 0.5 V and c) Process control with a path-dependent set-value 0.3 V(2 mm)–0.5 V(56 mm)–0.3 V(2 mm) [52].

Kruz [53], Kelly and Kampe [54], and Colaco and Vilar [55] suggested that the microstructural features and mechanical characteristics of DED parts depend partially on the solid-state transformation during the cooling step. However, it is reported that these transformations are driven by the thermal cycles that the material undergoes during the deposition. Since one of the most critical parameters that can affect the thermal history, and accordingly the microstructural evolution of metallic materials, is the cooling rate, several studies have been undertaken to estimate this parameter during DED of metallic materials. For this reason, several experiments [56,57], including analytical and numerical [58,59] approaches, have been developed to predict the effects of process variables on the cooling rate and consequently on the resulting microstructure in DED samples. For instance, Hofmeister et al. analyzed the thermal gradient and cooling rates in the regions near the melt pool through the monitoring of the melt pool via a digital video camera with thermal imaging techniques [60]. Griffith et al. evaluated the in situ thermal history of DED samples by inserting a thermocouple directly into the sample [42]. All of the experimental results showed that the formation of a very fine microstructure in DED components is a direct consequence of high cooling rates and the temperature gradient [56,57]. Gosh and Choi found that since the cooling rate significantly influences the primary cellular arm spacing (PCAS), it is possible to evaluate the thermal history and cooling rate of DED parts via PCAS analysis [61]. Therefore, they proposed an equation which describes the correlation between the PCAS and the thermal history of DED samples. Subsequently, several research studies have been conducted to investigate the correlation between the cooling rate (ε) and PCAS (λ), and outcomes reveal a linear relationship between $\log\lambda$ and $\log\varepsilon$ [62,63]. Bontha et al. also studied the correlation between dendrite morphology, temperature gradient, and solidification rate during the DED process [27]. Recently, Saboori et al. evaluated the PCAS of AISI 316L alloy produced via DED

at different distances from the substrate [37]. Thereafter, in their work, the cooling rate is estimated as a function of sample height using the PCAS values. It is found that by increasing the height of the sample up to the last layers, the PCAS values monotonously increase, and thereafter values drop suddenly when close to the previous layers (Figure 6).

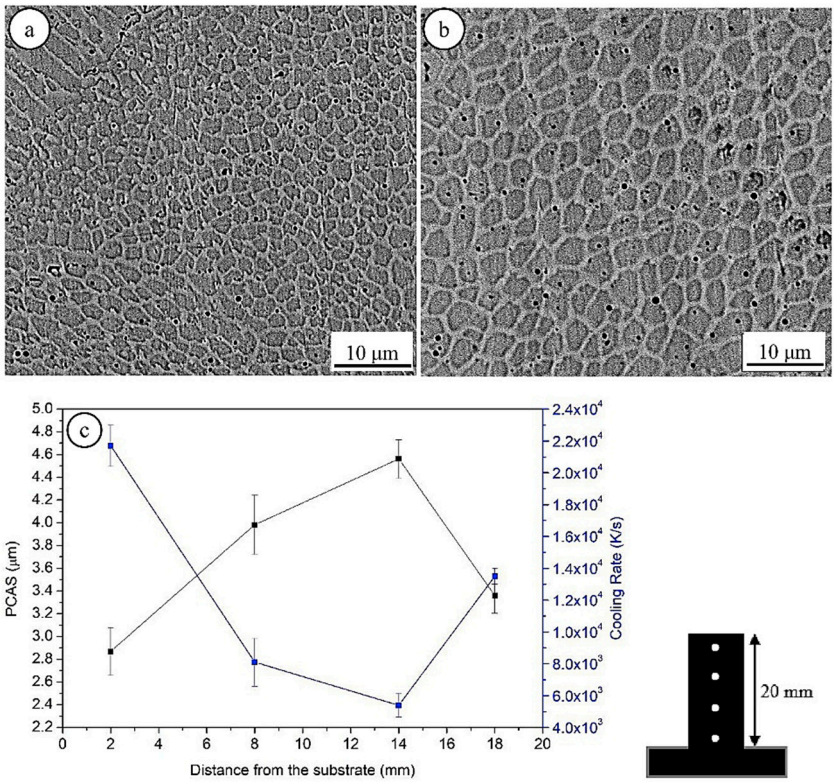

Figure 6. SEM images of DED AISI 316L at: (**a**) 2 mm, (**b**) 14 mm from the deposition/substrate interface, (**c**) primary cellular arm spacing (PCAS) and cooling rate as a function of the distance from the substrate [37].

As can be seen in Figure 6, the estimated cooling rate during DED of AISI 316L lies in the range of 10^3–10^4 K/s, which is in agreement with the typical cooling rate reported for the DED process [37,49,51]. Ma et al. compared the thermal history, cooling rate, and microstructural features of AISI 316L stainless steel produced by DED and laser powder bed fusion (LPBF) [49]. Indeed, in their work, five sets of process parameters are used to produce different cubes. Figure 7 shows the 3D view of the microstructures of the five different cubes; (a) low-power LPBF, (b) high-power LPBF, (c) small-size DED, (d) middle-size DED, and (e) large-size DED (Figure 7). As can be seen, the microstructure of all the samples is almost fully composed of cells, and all the dendrites have transformed into cells. Thereafter, their analyses revealed that the PCAS of each sample gradually increases with increasing the energy density (E) (Figure 8). Ma et al. also found that the solidification behavior of samples produced via DED is slightly different from that of specimens processed by LPBF. This means that by increasing the cooling rate, the solidification behavior is far from representing equilibrium conditions and accordingly results in a non-equilibrium microstructure. Moreover, it is revealed that lower cooling rate and lower supercooling in DED result in the formation of grains with a width and length 2–5 times coarser than those formed in the LPBF process.

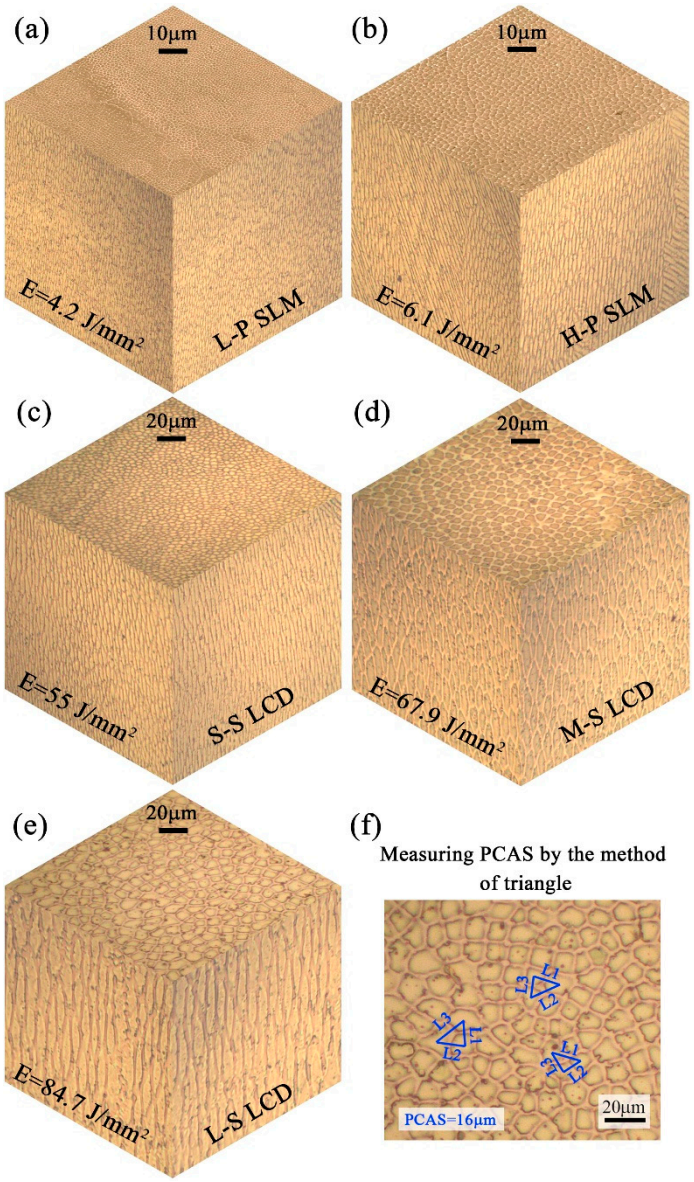

Figure 7. 3D composite view showing the cellular morphologies of the five kinds of typical samples at the processing parameters of (**a**) low-power laser powder bed fusion (LPBF), (**b**) high-power LPBF, (**c**) small-size DED, (**d**) middle-size DED, and (**e**) large-size DED. (**f**) Schematic sketch of measuring PCAS by the three-angle method [49].

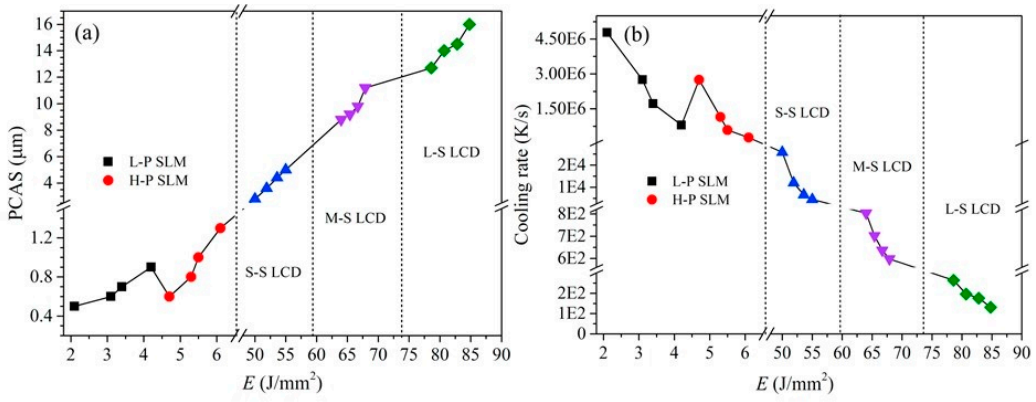

Figure 8. The effect of energy density E on the (**a**) PCAS and the (**b**) cooling rate of the as-forming AISI 316 L stainless steel samples at different processing parameters by LPBF and DED [49].

All of the experiments conducted in different studies proved that the size of dendrite arms would be in the range of a few microns. For example, Hofmeister et al. found that the average PCAS of AISI 316L produced via DED increased from 3 to 9 μm when the laser power increases [42]. Table 2 compares all the dendrite sizes that have been found in different studies. It should be highlighted that the evaluation of PCAS has been carried out using SEM images and three-angle method [37,49,64].

Table 2. A summary of PCAS reported for AISI 316L alloy processed by DED.

Author	Dimension (μm)	Ref.
Saboori et al.	2.8–4.8	[37]
Song et al.	1.3–3.0	[65]
Hofmeister et al.	3.25–8.68	[42]
Syed et al.	<5	[66]
Zheng et al.	8–20	[51]
Smugeresky et al.	2–15	[67]

In addition to the effect of cooling rate on microstructural morphology, it should be noted that this rapid solidification process also results in the phase composition of the microstructure of the samples in the as-built condition. In general, in the standard rapid solidified austenitic stainless steel, two distinct microstructural constituents can be achieved: austenite (γ) and δ-ferrite [68]. However, in order to predict the microstructure of the material from the phase composition point of view, some chemical composition-based phase diagrams, such as Schäffler and DeLong diagrams, are employed. The Schäffler diagram is the most accepted diagram used to predict the final microstructure of the material. In fact, this diagram is commonly employed to estimate the δ-ferrite content in the final microstructure of AISI 316L (Figure 9a). In addition to predicting δ-ferrite content, this diagram is also capable of predicting the existence of ferrite, martensite, and austenite phases in AISI 316L alloy as a function of the Cr and Ni equivalents [69]. However, it is reported that this diagram is not an exact diagram and, thus, the outcome is an approximation of the final δ-ferrite content [69]. Zhi'En et al. also studied the solidification mode of the AISI 316L alloy according to the role of alloying elements [41]. In their work, it is shown that by changing the ferrite stabilizer or austenite stabilizer content the solidification mode is different and, consequently, the final alloy can be either duplex or fully austenitic (Figure 9b).

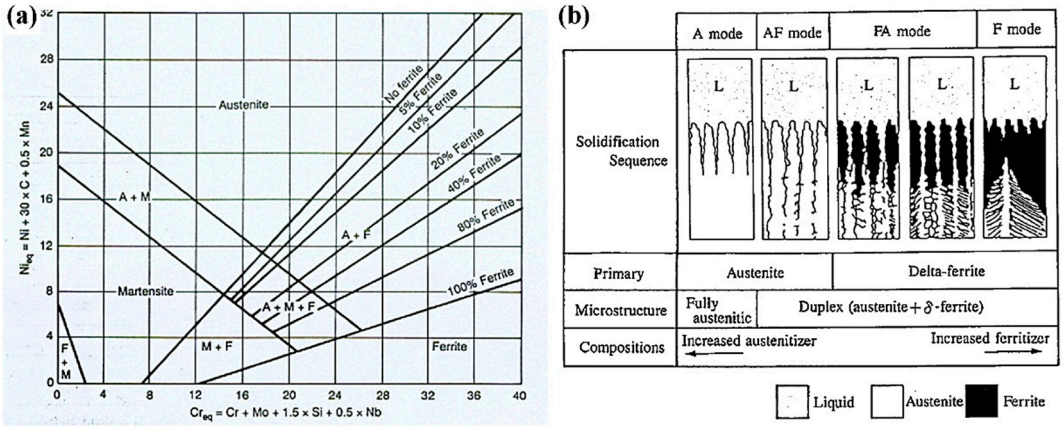

Figure 9. (**a**) Schaeffler's diagram and (**b**) austenitic steel solidification diagram [41].

However, it should be noted that this diagram has typically been used to predict the microstructure of corrosion-resistant steels with carbon content up to 0.25% after the welding process. Since the cooling rate is always higher than the welding process in the DED process, the solidification is not under equilibrium conditions. Therefore, it is highly recommended that, in addition to the conventional Schäffler diagram, another diagram, namely the pseudo-binary predictive phase

diagram, is used [70]. This means that once the theoretical δ-ferrite content is defined by Schäffler diagram, the WRC-1992 modified Cr and Ni equivalent formulas, which are shown on the X- and Y-axes of Figure 10 (a), can be used to place the steel being investigated in the pseudo-binary phase diagram (Figure 10).

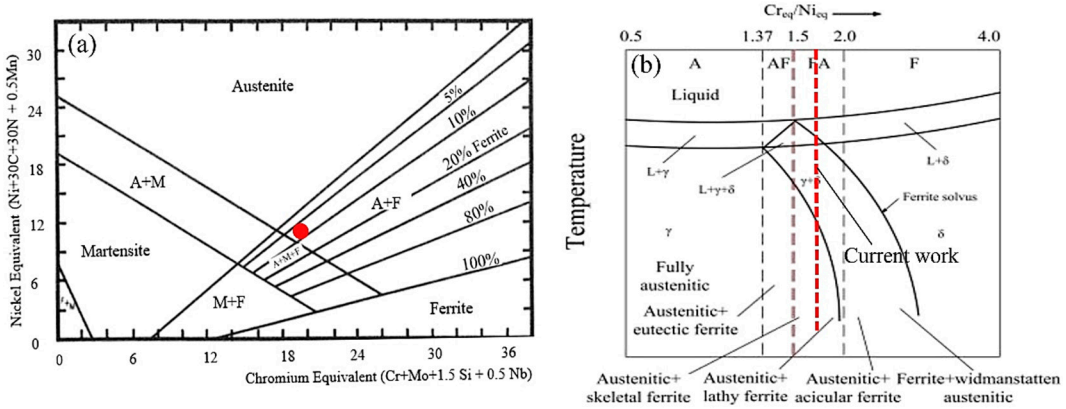

Figure 10. (**a**) Schaeffler constitution diagram showing the location of the composition of the AISI 316L stainless steel powders, (**b**) pseudo-binary phase diagram [37].

For instance, Tan et al. studied the microstructure of AISI 316L produced by DED. At first, they found that according to the chemical composition of the material and the Schäffler diagram, the estimated δ-ferrite content of the columnar boundary lies in the region of 20% δ-ferrite. The Cr_{eq} and Ni_{eq} of their DED AISI 316L suggest that the solidification of their material falls within the upper range of the austenitic-ferritic mode in such a way that an austenitic steel forms a predominantly austenitic microstructure with columnar δ-ferrite along the solidification direction (Figure 11) [41]. The δ-ferrite phase can be recognized by the higher Cr and Mo content. Milton et al. studied the microstructure of DED AISI 316L and revealed that Cr and Ni equivalent contents lie in the range of 5–10% δ-ferrite [71]. Zietala et al. also investigated DED of AISI 316L and found that intercellular δ-ferrite formed at sub-grain boundaries as a consequence of its enrichment of Cr and Mo, and depletion of Ni [35].

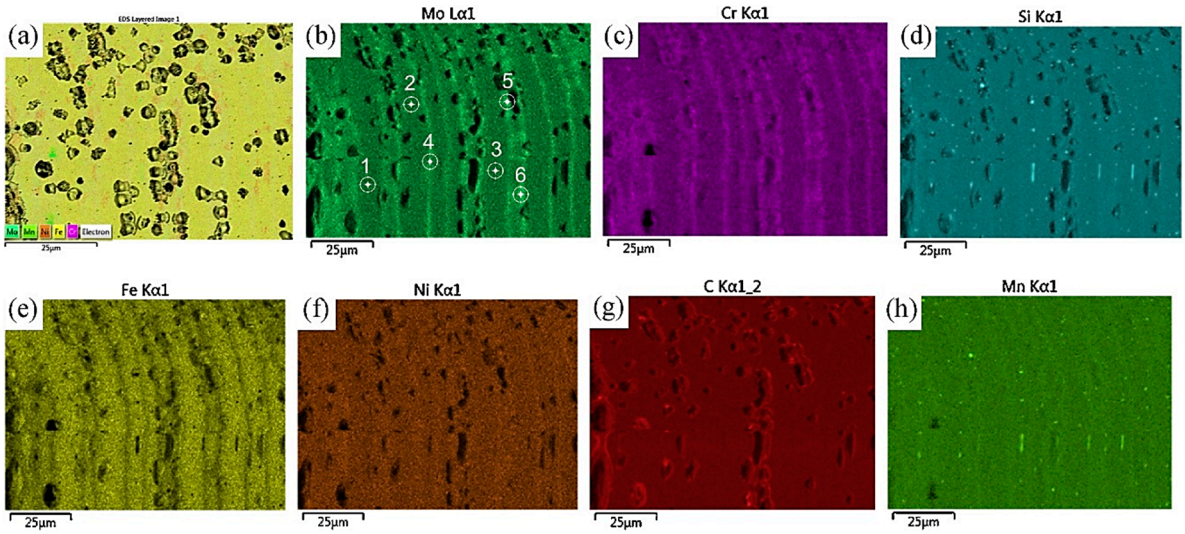

Figure 11. Element mapping for deposition body area: (**a**) layered element image, (**b**) molybdenum and target body, boundary element composition points, (**c**) chromium, (**d**) silicon, (**e**) iron, (**f**) nickel, (**g**) carbon, (**h**) manganese [41].

Formation of a duplex microstructure during DED of 316L was also revealed by Saboori et al. [37]. Indeed, they showed that the interdendritic arms are enriched in molybdenum and chromium,

which are δ-stabilizer elements. This elemental distribution can also be explained by the cooling rate of the process in which, during rapid solidification, austenite-promoting elements such as Ni and C are consumed to solidify the austenite phase and then the residual liquid phase is enriched in δ-stabilizer elements in the interdendritic regions.

Inclusion formation, such as of oxides rich in Si or Si and Mn, is an undesirable feature reported in DED of 316L [72]. These oxide structures are typically found during the ladle practice of high-content Mn/Si steels [73,74]. It is found that, due to their very high reactivity with oxygen, the formation of these oxides, even in secondary steelmaking, is difficult to avoid. Thus, in spite of using protective shielding gas to protect the melt pool, finding these kinds of oxides is not surprising. However, it should be noted that their detrimental effect on the components produced via DED with respect to the conventional steelmaking processes is relatively low, mainly owing to their final reduced size and spherical shape [37]. Lou et al. studied the oxide inclusion in laser AM of AISI 316L and reported their detrimental effect on the toughness and stress corrosion cracking behavior [75]. In fact, in their work, intergranular Si-rich and Si/Mn-rich oxides were found in as-built AISI 316L components (Figure 12). In another study, Ganesh et al. investigated the corrosion behavior of AISI 316L produced via DED [76]. They found that the presence of these oxides in the final microstructure weakens the corrosion resistance of the AISI 316L parts.

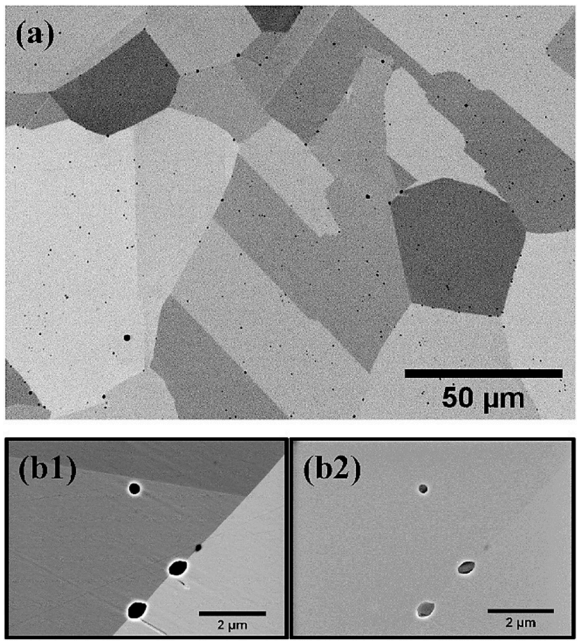

Figure 12. Oxide inclusions in the fully-recrystallized additive manufacturing (AM) AISI 316L stainless steel: (**a**) low magnification back-scattered electron image; (**b1**) high magnification back-scattered electron image; (**b2**) high magnification secondary electron image [75].

The size and the composition of the oxides found in AM AISI 316L samples, together with their effect on the material properties, are reported in Table 3. All these findings prove that in order to achieve the full potential of AISI 316L alloy in different applications, a more reliable deposition atmosphere should be used to comprehensively protect the melt pool and consequently reduce the oxide content of the alloy.

Table 3. A summary of the composition and size of oxides found in AM AISI 316L alloy.

AM Technology	Composition	Size	Effect	Ref.
LPBF	Si/Mn and Si/Mn/Mo rich oxides	50 nm–1 mm	Detrimental effect on toughness and stress corrosion cracking	[75]
DED	Cr_2O_3, MnO and SiO_2	0.31–0.49 µm	Higher yield strength	[77]

DED	Mn/Si-rich oxides	-	Detrimental effect on the elongation	[37]
DED	MnO and SiO_2	-	Possible effect on ductility reduction	[78]

However, it should be highlighted that since the size and quantity of these inclusions are normally lower than the resolution of the X-ray diffraction (XRD) analysis, they have mainly been analyzed via SEM and image analysis. The formation of these inclusions, mainly oxides, can change the failure behavior of material from ductile mode to brittle mode (as for the composite materials) [79,80].

3. Mechanical Properties

Mechanical properties can be considered one of the main indicators of the quality of an AM process. Hardness and tensile properties are, in fact, often used as key performance indicators (KPI) of AM components. From an industrial point of view, indeed, tensile samples are generally built together with AM components in order to validate the building process. Because of these reasons, mechanical properties of AM materials have been deeply investigated, and several tensile and hardness analyses of as-built DED AISI 316L samples obtained using different building or post-processing conditions are available in the literature.

Table 4 reports mechanical properties (i.e., Vickers hardness, Hv; yield strength, YS; ultimate strength, US; elongation, (ε)) of DED AISI 316L steel samples produced in different conditions (i.e., with several power (P) and scan speed (V) values, built along a perpendicular (V) or parallel (H) direction with respect to the building platform, with new powder or re-used powder, with Ar or N_2 shielding gas (SG) or a build chamber (BC) as protective atmosphere). These are compared with the tensile properties of AISI 316L samples obtained by conventional technologies (CT).

Table 4. A summary of the mechanical properties of AISI 316L samples produced via different technologies.

	P (W)	V (mm/s)	Direction	Gas	Hv	YS (MPa)	US (MPa)	ε (%)	H_c	Ref.
CT	Hot rolled				-	360	625	69	0.74	[81]
	Cast				170	310	620	45	1.00	[82]
Building parameters	1600	28	-	Ar BC	250	430	650	43	0.51	[49]
	3400	10	-	Ar BC	210	370	590	36	0.59	[49]
	4600	5	-	Ar BC	190	300	560	31	0.87	[49]
	*	2	H	Ar SG	310	505	625	19	0.24	[83]
	*	10	H	Ar SG	370	610	690	24	0.13	[83]
	600	*	H	Ar SG	350	585	655	18	0.12	[83]
	1400	*	H	Ar SG	320	545	620	19	0.14	[83]
Building direction	2000	8.3	V	-	-	415	770	6.5	0.86	[70]
	2000	8.3	H	-	-	580	900	4	0.55	[70]
	-	-	V	Ar SG	-	352	536	46	0.52	[83]
	-	-	H	Ar SG	-	558	639	21	0.15	[83]
	400	15	V	-	272	479	703	46	0.47	[35]
	400	15	H	-	289	576	776	33	0.35	[35]
	360	16	V	Ar BC	220–260	538–552	690–703	35–38	0.28–0.27	[84]
	360	16	H	Ar BC	220–260	448–455	545–634	4–25	0.22–0.39	[84]
Powder quality	-	-	H **	N_2 SG	-	469	628	31	0.34	[37]
	-	-	H ***	N_2 SG	-	458	652	16	0.42	[37]
Atmosphere	328	17	V	Ar BC	-	-	550	-	-	[39]
	360	16	V	Ar BC	222–260	448–455	545–634	4–25	0.22–0.39	[84]
	400	15	V	Ar SG	-	352	536	46	-	[83]
	-	-	H	N_2 SG	-	469 ± 3	628 ± 7	31 ± 2	0.34	[64]
	-	-	H	N_2 BC	-	530 ± 5	670 ± 6	34 ± 1	0.26	[64]

* The other building parameters were selected based on an orthogonal experimental design, the mechanical properties are intended to be the results of the application of the statistical method, ** Fresh powder, *** Re-used powder.

From the comparison of the data, it is evident that the tensile strength of DED AISI 316L samples is generally higher than that of conventionally manufactured steels. The reason for these peculiar mechanical properties of as-built AISI 316L parts can be found in their unique microstructure. The main factors that allow the achievements of high mechanical properties are the reduced grains and dendrite size, the presence of residual δ ferrite, and the presence of a dense dislocation network. These factors can also explain the low ductility values of the deposited parts. As previously discussed, these microstructural features are strictly correlated to the high cooling rate which the material undergoes while being processed.

The strengthening effect of the refined microstructure can be correlated to the well-known Hall–Petch equation that associates the material grain size and the YS as follows:

$$YS = YS_0 + \frac{k}{\sqrt{d}} \quad (1)$$

where YS_0 is the frictional stress resisting the motion of gliding dislocations in the absence of grain boundaries, d is the grain size, and k is a material constant.

Yan et al. suggested that for AM AISI 316L parts, there is a Hall–Petch type strengthening effect that correlates the YS to the cell size rather than to the grain size [73].

Yadollahi et al. claimed that metastable δ-ferrite also plays a vital role in the determination of the mechanical properties of DED AISI 316L samples as it is harder than the austenitic matrix [78]. Guo et al. also attributed the higher YS and US values obtained in their work to the presence of the high-temperature δ-ferrite phase. The ferritic phase causes a refinement of the microstructure and a consequent reduction of crack propagation [37]. The higher tensile properties associated with the presence of δ-ferrite are also correlated to the internal strain hardening that arises during the AM process caused by the different coefficient of thermal expansion of the two phases.

The high mechanical properties of AM AISI 316L were also ascribed to the high dislocation density of the as-built material [85]. Saeidi et al. observed a reduction in hardness of LPBF AISI 316L as a consequence of an annealing heat treatment. The microstructural analyses did not reveal any change in the microstructure but only a substantial reduction of the dislocation density at the cell boundaries and surrounding the non-metallic inclusions. The dislocation networks were then considered responsible for the high mechanical properties of as-built AM parts [85].

Several authors also highlighted that the plastic region of DED AISI 316L samples is relatively flat, indicating that these samples have a low strain hardening ability with respect to conventionally processed samples [39,84,86]. The strain hardening ability (Hc) is generally calculated as [86]:

$$H_c = \frac{(US - YS)}{YS} \quad (2)$$

By comparing the tensile data of DED AISI 316L steel samples reported in Table 4, it can be noted that there is a wide variation in their mechanical properties. Vickers hardness values, for example, vary between 190 and 370 HV, while the US values fall in the range 536–900 MPa. Nonetheless, the strongest variations can be found in the YS and the ε values, which vary from 300 to 610 MPa and from 4% to 46%, respectively. These discrepancies are generally due to the AM building conditions, powder quality, and tensile sample direction and geometry. Consequently, most of the considered studies related to the mechanical properties of these materials were focused on the understanding of the effect of the building conditions on the YS, US, and ε values. The main investigated aspects are described and summarized here.

3.1. Building Parameters

It is well-known that the DED building parameters, such as laser power, scan speed, and powder feeding rate are key factors that determine the quality of components. The identification of the most suitable combination of these process parameters can assure not only the achievement of dense samples but also can result in the formation of the desired microstructure and mechanical properties [31,87]. As a result, many authors have investigated the effect of combinations of process parameters on mechanical properties of components. In the first rows of Table 4, data related to samples built

with different parameters are reported according to the paper of Ma et al. Considering that other DED parameters and machine configurations, such as laser spot size and standoff distance, can also affect the mechanical properties, data recorded in different research studies are not compared with each other. In this way it is possible to underline the influence of process parameters on mechanical behavior of DED parts without neglecting some factors specific to the system employed in each study.

As demonstrated by Ma et al., there is a clear correlation between the tensile properties of DED AISI 316L steel samples and the delivered energy density. The lowest YS, US, and ε (300 MPa, 560 MPa, and 31%, respectively) values were in fact obtained with the highest power and the lowest scan speed (Table 4). The authors explained this effect through the correlation that exists between YS, PCAS, and the width and length of the columnar grains. As previously described, these microstructural features are strictly connected to the cooling rate and thermal gradient, generally controlled trough the building parameters [49].

Similar results were obtained by Zhang et al., who studied the effect of the laser power and scan speed on the hardness values and tensile properties of DED AISI 316L samples [83]. It was demonstrated that in all the samples, the higher the laser power, the lower are YS and US, while the opposite is true for the scanning speed (Table 4). This effect was also explained by the different cooling rate of the materials under different building conditions. High power and low scan speed lead, in fact, to the formation of larger melt pools and lower cooling rate. Low power and high scan speed, on the contrary, lead to the formation of smaller melt pools that solidify with an extremely high cooling rate. The authors did not report, however, any clear correlation between energy input and elongation.

3.2. Building Direction

The correlation between the building direction and tensile properties is a crucial aspect in the determination of the mechanical properties of AM samples. The anisotropy of the microstructure and the presence of some defects affect the stress–strain curve [49]. The main factors related to the building direction that have an effect on the tensile properties can be listed as follows:

- Grain morphology
- Texture
- Elongated dendrites
- Lack of fusion defects

Guo et al. investigated the impact of the building direction of the mechanical properties and showed that the highest mechanical properties (YS, US, and ε) were observed in the H samples (Table 4). The authors attributed this difference to the superior metallurgical bonding of these samples along the tensile direction. Horizontal samples have at least one layer in which the deposition direction is parallel to the tensile direction. The consolidated scan tracks deposited along the direction parallel to the tensile direction act, therefore, as fibers that reinforce the materials during the tensile tests [70]. On the contrary, the V samples might contain some critical elongated defects perpendicular to the tensile direction due to a lack of fusion between different layers, which can be detrimental during the tensile test.

Similar results were obtained by Ziętala et al. and Zhang et al., who confirmed that the highest YS and US were achieved in the H direction. These authors, however, observed higher elongation values in the V samples (Table 4) [35,83]. The higher elongation of vertical samples was attributed by Zhang et al. to the improved ductility due to the dendrites along the growth direction [83]. Yang et al. also analyzed the tensile properties of DED AISI 316L samples (both vertical and horizontal) extracted from a more complex geometry and also obtained lower YS and US in the vertical samples [84]. It is important to underline that these data showed a large scattering, probably because of the different distribution of defects due to the complex geometry from which samples were extracted.

In this case, the vertical samples had a drastically lower elongation value, which was attributed to the delamination phenomenon that was clearly detectable by the fracture surface analyses (Figure 13). The fracture surface analysis indicates that the V and H samples showed different deformation

characteristics. The vertical samples had a very reduced necking and displayed a fracture surface characterized by some features, such as unmelted particles and smooth areas, that indicate an incomplete fusion during the building process. The horizontal samples, on the contrary, have a strong necking phenomenon and display the typical ductile fracture surface characterized by fine dimples with a size comparable to the PCAS.

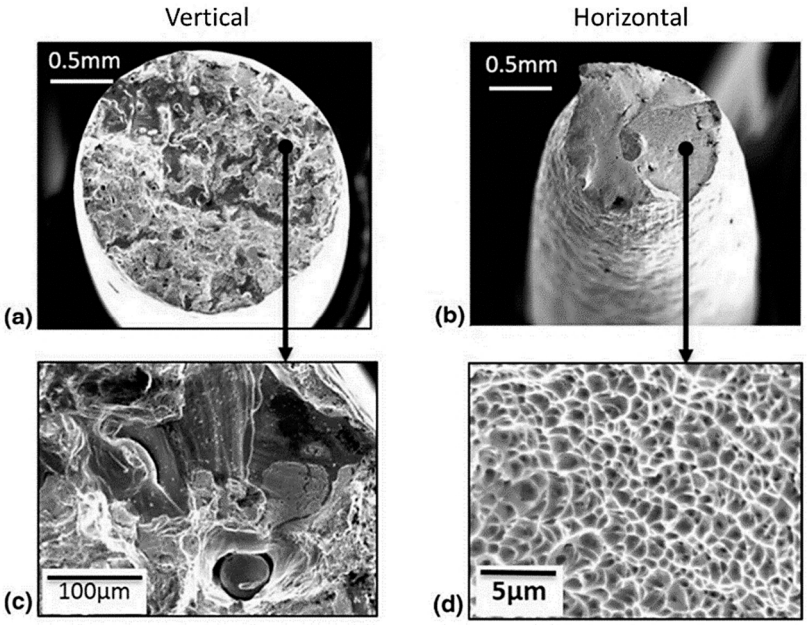

Figure 13. SEM micrographs of the tensile fracture surface: (**a**,**c**) vertical; (**b**,**d**) horizontal [84].

In general, based on these results, it can be concluded that the highest YS and US are generally achieved in the horizontally built samples, and the effect of building direction on the elongation value is still controversial. This discrepancy can be probably related to the other building conditions, as well as the porosity and inclusion content, together with the effect of other strengthening phenomena.

In the case of horizontal samples, however, further studies are needed to investigate the effect of the distance from the substrate on the tensile properties. Wang et al. demonstrated that YS and US of DED 304L stainless steel increase as the distance from the substrate decreases due to the different microstructures that solidify based on the cooling rate [31].

3.3. Powder Quality

It is well known that powder quality plays a fundamental role in the quality of the AM processes as it influences not only consolidation phenomena and consequently porosity contents, but also microstructure and alloy composition.

Saboori et al. studied the effect of powder recycling on the quality of DED AISI 316L parts [37]. In their comparison, the authors found that the mechanical properties of DED AISI 316L samples built with fresh and recycled powders were different (Table 4). The main difference was found in the elongation values that resulted in being very low for the samples built with the recycled powder. This reduction in ε was mainly attributed to the presence of large non-metallic inclusions, which were found to be Mn and Si-based oxides (Figure 14a,b). As demonstrated from the comparison with Figure 14c,d, the inclusions were observed on the recycled particles, suggesting that the oxidation might arise on the particles that are partially heated by the laser beam and exit from the protected atmosphere generated by the shielding gas.

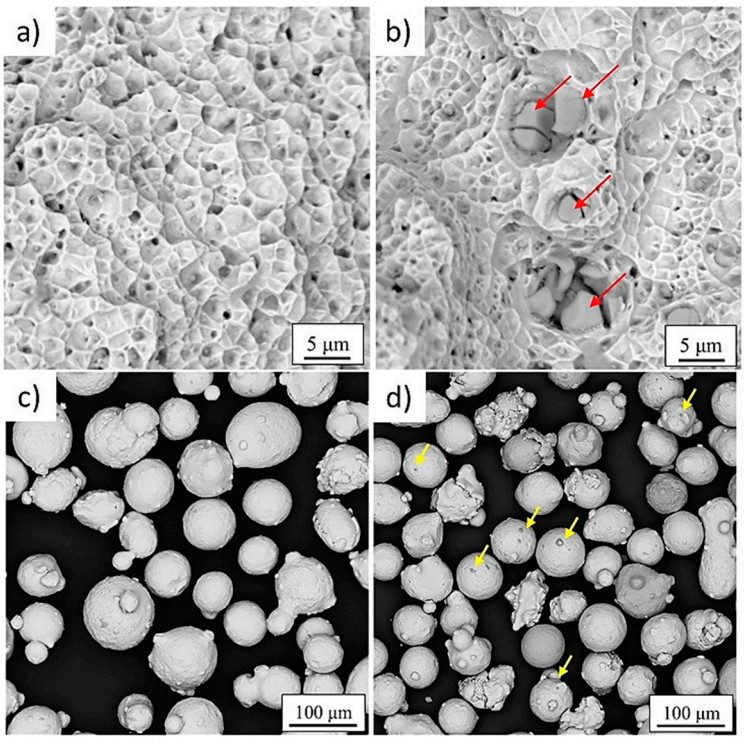

Figure 14. A summary of the tensile fracture morphologies of AISI 316L stainless steel samples produced by DED using (**a**) fresh powder and (**b**) recycled powder. SEM images of (**c**) fresh and (**d**) recycled AISI 316L powders [37].

This marked effect of the oxide content and powder quality on the final mechanical properties of the DED AISI 316L samples suggests that the production of samples in a protective chamber may enhance the quality of the recycled powder, with the deposition allowing the production of parts with higher mechanical properties.

3.4. Building Atmosphere

A close look at Table 4 highlights that DED AISI 316L samples can be built in different atmospheres, such as argon or nitrogen. Furthermore, the protective atmosphere can be generated in two main ways. The first is the use of a simple shielding gas that locally protects the molten material from oxidation, while the second involves the usage of a protective chamber filled with an inert gas.

Aversa et al. recently compared the mechanical properties of DED AISI 316L built using a N_2 shielding gas or using a N_2-filled build chamber. The results showed that very high mechanical properties can be obtained in both conditions and that the use of the Glove Box (GB) allows the achievement of higher YS, US, and ε (Table 4). This effect was attributed to the reduced size of the oxides and the higher N content of BC samples, which have a strengthening effect [64].

The inert gas composition may also have an effect on both the processability of the alloy and its microstructure and mechanical properties. These effects have not yet been investigated in the AM field but were recently studied and reported in the welding literature [88]. In the case of AISI 316L production by DED, it is important to consider that nitrogen is a γ-stabilizer and therefore reduces the high-temperature δ-ferrite phase content which, as previously stated, plays a vital role in the determination of mechanical properties of the final parts. Furthermore, N is an important alloying element for austenitic stainless steel and using it as protective gas might increase the mechanical properties of DED AISI 316L [89].

3.5. Heat Treatment

It is well-known that as-built AM samples and components are characterized by the presence of high residual stresses due to the complex thermal history to which the material is subjected while being processed. Because of this reason, AM components usually undergo specific post-heat treatments that allow the reduction of internal stresses and the homogenization of microstructures.

However, to date, only a small number of studies have been carried out on the effect of the stress-relieving/annealing heat treatments on DED AISI 316L properties [78,90]. The main tensile tests results are summarized in Table 5. The data show that, typically, the YS and US of DED AISI 316L parts are reduced as a consequence of heat treatments. This reduction was mainly attributed to the decrease in the δ-ferrite content [78] and to the reduction of the dislocation density [85]. Furthermore, it is also interesting to underline that a higher strain hardening was observed in heat-treated samples; this can also be due to different dislocation contents.

Table 5. Tensile properties of DED AISI 316L samples in the as-built and heat-treated conditions.

P (W)	V (mm/s)	Conditions	YS (MPa)	US (MPa)	ε (%)	H_c	Ref.
360	8.5	As-built	405–415	620–660	32–40	0.49–0.63	[78]
		1150 °C 2 h Air quenched	325–355	600–620	42–43	0.69–0.91	
380	-	As-built	-	720	56		[90]
		1060 °C 1 h Vacuum treated		605	78		

Despite the differences in the mechanical properties, the fracture surfaces of as-built and heat-treated samples are usually very similar (Figure 15). Morrow et al. reported, for example, a ductile fracture surface characterized by the presence of micrometric dimples for both as-built and heat-treated samples [90]. Moreover, in both samples, extremely fine Mn/Si oxide particles can be detected in the dimples.

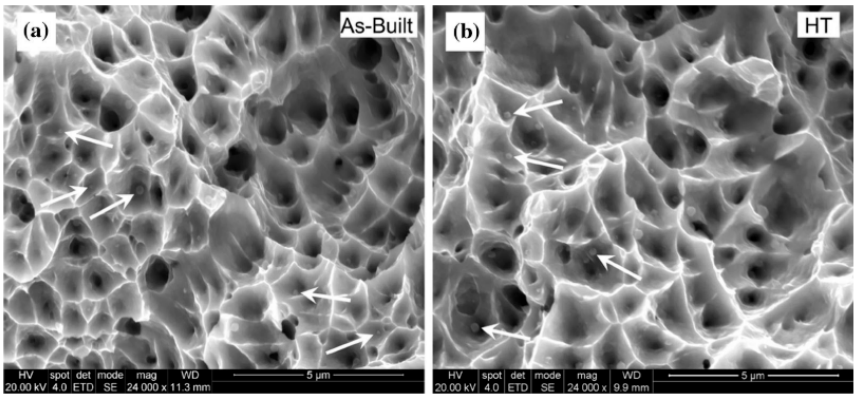

Figure 15. Fracture surfaces of AISI 316L stainless steel: (**a**) as-built and (**b**) heat-treated. Arrows mark a few of the many examples of fine particles observed resting inside ductile dimples throughout the fracture surface [90].

Other more specific mechanical properties of DED 316L were also recently investigated by several authors. Xue et al. and Ganesh et al. studied, for example, the DED 316L impact and fatigue performance of as-built parts [91,92]. Their main finding is that DED samples have a Charpy impact energy and fatigue crack growth rate similar to conventionally manufactured samples. Furthermore, crack propagation in DED samples is transgranular and accompanied by a strain-induced martensite formation

4. Conclusions

As one of the most employed AM technologies, DED offers excellent potential for the production of complex shape components, which are arduous to produce through conventional processes. AISI 316L is a well-known austenitic stainless with high corrosion resistance, as well as good mechanical

properties, which make this alloy an excellent candidate for several sectors, such as the automotive and petrochemical industries. This review article summarizes the latest research carried out to evaluate microstructures and mechanical properties of AISI 316L stainless steel processed by DED. The correlation between the DED process parameters, thermal history, and microstructure of AISI 316L materials is discussed in detail. It is found that most previous works have aimed to determine the optimal process parameters for the DED production of AISI 316L components. These efforts have been taken in order to improve the density and mechanical properties of AISI 316L components produced via the DED process through the control of their microstructure. However, it should be highlighted that, in spite of this research effort, a number of challenges remain that should be considered and addressed in further investigations. The main challenges are associated with the correlation among DED process parameters, thermal history, microstructure, and mechanical characteristics of the DED AISI 316L parts. To date, investigations of DED AISI 316L materials have demonstrated that:

- Optimization of process parameters is a vital step that should be carried out carefully in order to achieve defect-free components with desired final characteristics.
- DED process parameters markedly affect the cooling rate, thermal gradient and, accordingly, thermal history and porosity content of the parts. It is well known that the quality of DED parts is chiefly determined by the process parameters, as well as the starting powder (particle size and chemical composition).
- Regarding the process parameters, the most important are laser power, scan speed, powder feed rate, building atmosphere, and deposition pattern. All these parameters influence the microstructure. The very high cooling rates of DED processes, with values around 10^3–10^4 °C/s, involve the formation of columnar and cellular structures based on the direction of thermal flux. It was reported that the columnar structures are dominant throughout the specimens, while the cellular structures are predominant in the last deposited layers.
- It is found that, the finer the PCAS, the higher the cooling rates. The high cooling rates generate very fine dendritic structures, as well as high dislocation densities, resulting in higher mechanical strength.
- The microstructure is composed of austenite γ and δ-ferrite, which is typically formed with the sub-grain structures enriched in Cr and Mo (δ-ferrite stabilize elements).
- Oxide formation is an undesired feature that affects the production of AISI 316L by the DED process. It is found that the presence of oxides can negatively affect the mechanical properties, even though an inert gas atmosphere is employed.
- The aforementioned microstructure features lead to materials with higher strength and lower ductility values with respect to conventionally processed AISI 316L stainless steel.
- Anisotropy in the tensile properties of DED components is widely detected; typically, the specimens produced along a direction parallel to the building platform present higher YS and US than specimens built perpendicular to the building platform. This can be attributed to different microstructure and thermal history, although there is a lack of extensive studies.
- Grain morphology, texture, elongated dendrites, and lack of fusion defects are found to be the main factors associated with the perpendicular building direction that have an effect on the tensile properties of DED AISI 316L components.
- Variations of the chemical composition associated with the recycling of the starting powder can influence microstructure and mechanical properties. In particular, the recycling of the powder can result in a higher oxide concentration (Mn and Si oxides) and, consequently, in a lower ductility of the final DED AISI 316L parts.

Author Contributions: To write this review article, A.S., A.A., and G.M. collected the papers, analyzed the literature, and wrote the article; S.B., M.L., and P.F. revised the article technically and scientifically. All authors have read and agreed to the published version of the manuscript.

Funding: This research received no external funding.

Conflicts of Interest: The authors declare no conflict of interest.

References

1. Saboori, A.; Gallo, D.; Biamino, S.; Fino, P.; Lombardi, M. An Overview of Additive Manufacturing of Titanium Components by Directed Energy Deposition: Microstructure and Mechanical Properties. *Appl. Sci*. **2017**, *7*, 883, doi:10.3390/app7090883.
2. Marchese, G.; Parizia, S.; Rashidi, M.; Saboori, A.; Manfredi, D.; Ugues, D.; Lombardi, M.; Hryha, E.; Biamino, S. The role of texturing and microstructure evolution on the tensile behavior of heat-treated Inconel 625 produced via laser powder bed fusion. *Mater. Sci. Eng. A* **2020**, *769*, 138500, doi:10.1016/j.msea.2019.138500.
3. Liou, F.; Slattery, K.; Kinsella, M.; Newkirk, J.W.; Landers, R.; Chou, H.-N. Applications of a hybrid manufacturing process for fabrication of metallic structures. *Rapid Prototyp. J.* **2007**, *13*, 236–244, doi:10.1108/13552540710776188.
4. Bosio, F.; Saboori, A.; Lacagnina, A.; Librera, E.; De Chirico, M.; Biamino, S.; Fino, P.; Lombardi, M. Directed energy deposition of 316L steel: Effect of type of powders and gas related parameters. In Proceedings of the Euro PM2018 Congress & Exhibition, Bilbao, Spain, 14–18 October 2018; pp. 1–6.
5. Galati, M.; Iuliano, L. A literature review of powder-based electron beam melting focusing on numerical simulations. *Addit. Manuf*. **2018**, *19*, 1–20, doi:10.1016/j.addma.2017.11.001.
6. Aristizabal, M.; Jamshidi, P.; Saboori, A.; Cox, S.C.; Attallah, M.M. Laser powder bed fusion of a Zr-alloy: Tensile properties and biocompatibility. *Mater. Lett.* **2020**, *259*, 126897, doi:10.1016/j.matlet.2019.126897.
7. Barros, R.; Silva, F.J.G.; Gouveia, R.; Saboori, A.; Marchese, G.; Biamino, S.; Salmi, A.; Atzeni, E. Laser Powder Bed Fusion of Inconel 718: Residual Stress Analysis Before and After Heat Treatment. *Metals* **2019**, *9*, 1290, doi:10.3390/met9121290.
8. Marchese, G.; Bassini, E.; Aversa, A.; Lombardi, M.; Ugues, D.; Fino, P.; Biamino, S. Microstructural Evolution of Post-Processed Hastelloy X Alloy Fabricated by Laser Powder Bed Fusion. *Materials* **2019**, *12*, 486, doi:10.3390/ma12030486.
9. Frazier, W.E. Metal Additive Manufacturing: A Review. *J. Mater. Eng. Perform.* **2014**, *23*, 1917–1928, doi:10.1007/s11665-014-0958-z.
10. Del Guercio, G.; Galati, M.; Saboori, A.; Fino, P.; Iuliano, L. Microstructure and Mechanical Performance of Ti–6Al–4V Lattice Structures Manufactured via Electron Beam Melting (EBM): A Review. *Acta Met. Sin.* **2020**, *33*, 183–203, doi:10.1007/s40195-020-00998-1.
11. Mazzucato, F.; Valente, A.; Lai, M.; Biamino, S.; Lombardi, M.; Lombardi, M. Monitoring Approach to Evaluate the Performances of a New Deposition Nozzle Solution for DED Systems. *Technologies* **2017**, *5*, 29, doi:10.3390/technologies5020029.
12. Gibson, I.; Rosen, D.; Stucker, B. Directed Energy Deposition Processes. *Addit. Manuf. Technol.* 2015, 245–268, doi:10.1007/978-1-4939-2113-3_10.
13. Keicher, D.M.; Miller, W.D. LENSTM moves beyond RP to direct fabrication. *Met. Powder Rep*. **1998**, *53*, 26–28.
14. Wołosz, P.; Baran, A.; Polański, M. The influence of laser engineered net shaping (LENS™) technological parameters on the laser deposition efficiency and properties of H13 (AISI) steel. *J. Alloys Compd*. **2020**, *823*, 153840, doi:10.1016/j.jallcom.2020.153840.
15. Petrat, T.; Graf, B.; Gumenyuk, A.; Rethmeier, M. Laser Metal Deposition as Repair Technology for a Gas Turbine Burner Made of Inconel 718. *Phys. Procedia* **2016**, *83*, 761–768, doi:10.1016/j.phpro.2016.08.078.
16. Zhang, Y.; Yang, L.; Lu, W.; Wei, D.; Meng, T.; Gao, S. Microstructure and elevated temperature mechanical properties of IN718 alloy fabricated by laser metal deposition. *Mater. Sci. Eng. A* **2020**, *771*, 138580.
17. Weerasinghe, V.M.; Steen, W.M. Laser Cladding By Powder Injection. In Proceedings of the 1st International Conference on Lasers in Manufacturing, East Sussex, UK, 1983; pp. 125–132.
18. Weerasinghe,V.M.; Steen, W.M. Laser Cladding With Blown Powder. *Met. Constr*. **1987**, *19*, 581–585.
19. Mazumder, J.; Choi, J.; Nagarathnam, K.; Koch, J.; Hetzner, D. The direct metal deposition of H13 tool steel for 3-D components. *JOM* **1997**, *49*, 55–60, doi:10.1007/bf02914687.
20. Chen, B.; Su, Y.; Xie, Z.; Tan, C.; Feng, J. Development and characterization of 316L/Inconel625 functionally graded material fabricated by laser direct metal deposition. *Opt. Laser Technol*. **2020**, *123*, 105916, doi:10.1016/j.optlastec.2019.105916.
21. Zhang, J.; Liou, F. Adaptive Slicing for a Multi-Axis Laser Aided Manufacturing Process. *J. Mech. Des.* **2004**, *126*, 254–261, doi:10.1115/1.1649966.

22. Milewski, J.; Lewis, G.; Thoma, D.; Keel, G.; Nemec, R.; Reinert, R. Directed light fabrication of a solid metal hemisphere using 5-axis powder deposition. *J. Mater. Process. Technol*. **1998**, *75*, 165–172, doi:10.1016/s0924-0136(97)00321-x.
23. Wu, X.; Liang, J.; Mei, J.; Mitchell, C.; Goodwin, P.; Voice, W. Microstructures of laser-deposited Ti–6Al–4V. *Mater. Des*. **2004**, *25*, 137–144, doi:10.1016/j.matdes.2003.09.009.
24. Shao, S.; Yadollahi, A.; Bian, L.; Thompson, S.M. An overview of Direct Laser Deposition for additive manufacturing; Part II: Mechanical behavior, process parameter optimization and control. *Addit. Manuf.* **2015**, *8*, 12–35, doi:10.1016/j.addma.2015.07.002.
25. Saboori, A.; Aversa, A.; Marchese, G.; Biamino, S.; Lombardi, M.; Fino, P. Application of Directed Energy Deposition-Based Additive Manufacturing in Repair. *Appl. Sci.* **2019**, *9*, 3316, doi:10.3390/app9163316.
26. Mazumder, J.; Dutta, D.; Kikuchi, N.; Ghosh, A. Closed loop direct metal deposition: Art to part. *Opt. Lasers Eng.* **2000**, *34*, 397–414, doi:10.1016/s0143-8166(00)00072-5.
27. Bontha, S.; Klingbeil, N.; Kobryn, P.A.; Fraser, H.L. Thermal process maps for predicting solidification microstructure in laser fabrication of thin-wall structures. *J. Mater. Process. Technol*. **2006**, *178*, 135–142, doi:10.1016/j.jmatprotec.2006.03.155.
28. Bontha, S.; Klingbeil, N.; Kobryn, P.A.; Fraser, H.L. Effects of process variables and size-scale on solidification microstructure in beam-based fabrication of bulky 3D structures. *Mater. Sci. Eng. A* **2009**, *513*, 311–318, doi:10.1016/j.msea.2009.02.019.
29. Zadi-Maad, A.; Rohib, R.; Irawan, A. Additive manufacturing for steels: A review. *IOP Conf. Series: Mater. Sci. Eng*. **2018**, *285*, 12028.
30. Saboori, A.; Tusacciu, S.; Busatto, M.; Lai, M.; Biamino, S.; Fino, P.; Lombardi, M. Production of Single Tracks of Ti-6Al-4V by Directed Energy Deposition to Determine the Layer Thickness for Multilayer Deposition. *J. Vis. Exp.* **2018**, e56966, doi:10.3791/56966.
31. Wang, Z.; Palmer, T.A.; Beese, A.M. Effect of processing parameters on microstructure and tensile properties of austenitic stainless steel 304L made by directed energy deposition additive manufacturing. *Acta Mater.* **2016**, *110*, 226–235, doi:10.1016/j.actamat.2016.03.019.
32. Majumdar, J.D.; Pinkerton, A.; Liu, Z.; Manna, I.; Li, L. Mechanical and electrochemical properties of multiple-layer diode laser cladding of 316L stainless steel. *Appl. Surf. Sci.* **2005**, *247*, 373–377, doi:10.1016/j.apsusc.2005.01.131.
33. Sun, G.F.; Shen, X.; Wang, Z.; Zhan, M.; Yao, S.; Zhou, R.; Ni, Z. Laser metal deposition as repair technology for 316L stainless steel: Influence of feeding powder compositions on microstructure and mechanical properties. *Opt. Laser Technol*. **2019**, *109*, 71–83, doi:10.1016/j.optlastec.2018.07.051.
34. Bertoli, U.S.; Guss, G.; Wu, S.; Matthews, M.; Schoenung, J.M. In-situ characterization of laser-powder interaction and cooling rates through high-speed imaging of powder bed fusion additive manufacturing. *Mater. Des.* **2017**, *135*, 385–396, doi:10.1016/j.matdes.2017.09.044.
35. Ziętala, M.; Durejko, T.; Polański, M.; Kunce, I.; Płociński, T.; Zieliński, W.; Łazińska, M.; Stępniowski, W.; Czujko, T.; Kurzydłowski, K.J.; et al. The microstructure, mechanical properties and corrosion resistance of 316L stainless steel fabricated using laser engineered net shaping. *Mater. Sci. Eng. A* **2016**, *677*, 1–10, doi:10.1016/j.msea.2016.09.028.
36. Yadollahi, A.; Seely, D.; Patton, B.; Shao, S. Microstructural Features and Mechanical Properties of 316L Stainless Steel fabricated by Laser Additive Manufacture. In Proceedings of the 56th AIAA/ASCE/AHS/ASC Structures, Structural Dynamics, and Materials Conference, Kissimmee, FL, USA, 9 January 2015, doi:10.2514/6.2015-1355.
37. Saboori, A.; Aversa, A.; Bosio, F.; Bassini, E.; Librera, E.; De Chirico, M.; Biamino, S.; Ugues, D.; Fino, P.; Lombardi, M. An investigation on the effect of powder recycling on the microstructure and mechanical properties of AISI 316L produced by Directed Energy Deposition. *Mater. Sci. Eng. A* **2019**, *766*, 138360, doi:10.1016/j.msea.2019.138360.
38. Saboori, A.; Piscopo, G.; Lai, M.; Salmi, A.; Biamino, S. An investigation on the effect of deposition pattern on the microstructure, mechanical properties and residual stress of 316L produced by Directed Energy Deposition. *Mater. Sci. Eng. A* **2020**, *780*, 139179, doi:10.1016/j.msea.2020.139179.
39. Zheng, B.; Haley, J.; Yang, N.; Yee, J.; Terrassa, K.; Zhou, Y.; Lavernia, E.; Schoenung, J. On the evolution of microstructure and defect control in 316L SS components fabricated via directed energy deposition. *Mater. Sci. Eng. A* **2019**, *764*, 138243, doi:10.1016/j.msea.2019.138243.

40. Terrassa, K.L.; Smith, T.R.; Jiang, S.; Sugar, J.D.; Schoenung, J.M. Improving build quality in Directed Energy Deposition by cross-hatching. *Mater. Sci. Eng. A* **2019**, *765*, 138269, doi:10.1016/j.msea.2019.138269.
41. Tan, Z.E.; Pang, J.H.L.; Kaminski, J.; Pepin, H.; Zhi'En, E.T. Characterisation of porosity, density, and microstructure of directed energy deposited stainless steel AISI 316L. *Addit. Manuf.* **2019**, *25*, 286–296, doi:10.1016/j.addma.2018.11.014.
42. Griffith, M.; Schlienger, M.; Harwell, L.; Oliver, M.; Baldwin, M.; Ensz, M.; Essien, M.; Brooks, J.; Robino, C.; Smugeresky, J.; et al. Understanding thermal behavior in the LENS process. *Mater. Des*. **1999**, *20*, 107–113, doi:10.1016/s0261-3069(99)00016-3.
43. Kobryn, P.A.; Semiatin, S.L. Mechanical properties of laser-deposited Ti-6Al-4V. In Proceedings of the Solid Freeform fabrication proceedings, Austin, August 6, 2001, pp. 179–186.
44. Saboori, A.; Biamino, S.; Lombardi, M.; Tusacciu, S.; Busatto, M.; Lai, M.; Fino, P. How the nozzle position affects the geometry of the melt pool in directed energy deposition process. *Powder Met*. **2019**, *62*, 213–217, doi:10.1080/00325899.2019.1627490.
45. Selcuk,C. Laser metal deposition for powder metallurgy parts. *Powder Met*. **2011**, *54*, 94–99.
46. Vilar, R. Laser cladding. *Laser Appl*. **2001**, *11*, 64–79.
47. Ensz, M.; Griffith, M.; Hofmeister, W.; Philliber, J.A.; Smugeresky, J.; Wert, M. *Investigation of Solidification in the Laser Engineered Net Shaping (LENS) Process*; Sandia National Laboratories: Livermore, CA, USA, 1999.
48. Debroy, T.; Wei, H.; Zuback, J.; Mukherjee, T.; Elmer, J.; Milewski, J.; Beese, A.M.; Wilson-Heid, A.; De, A.; Zhang, W. Additive manufacturing of metallic components—Process, structure and properties. *Prog. Mater. Sci*. **2018**, *92*, 112–224, doi:10.1016/j.pmatsci.2017.10.001.
49. Ma, M.; Wang, Z.; Zeng, X. A comparison on metallurgical behaviors of 316L stainless steel by selective laser melting and laser cladding deposition. *Mater. Sci. Eng. A* **2017**, *685*, 265–273, doi:10.1016/j.msea.2016.12.112.
50. El Kadiri, H.; Wang, L.; Horstemeyer, M.F.; Yassar, R.S.; Berry, J.T.; Felicelli, S.; Wang, P.T. Phase transformations in low-alloy steel laser deposits. *Mater. Sci. Eng. A* **2008**, *494*, 10–20, doi:10.1016/j.msea.2007.12.011.
51. Zheng, B.; Zhou, Y.; Smugeresky, J.; Schoenung, J.; Lavernia, E. Thermal Behavior and Microstructural Evolution during Laser Deposition with Laser-Engineered Net Shaping: Part I. Numerical Calculations. *Met. Mater. Trans. A* **2008**, *39*, 2228–2236, doi:10.1007/s11661-008-9557-7.
52. Bi, G.; Gasser, A.; Wissenbach, K.; Drenker, A.; Poprawe, R. Characterization of the process control for the direct laser metallic powder deposition. *Surf. Coatings Technol*. **2006**, *201*, 2676–2683, doi:10.1016/j.surfcoat.2006.05.006.
53. Kurz, W. Solidification Microstructure-Processing Maps: Theory and Application. *Adv. Eng. Mater. Banner*. **2001**, *3*, 443–452.
54. Kelly, S.M.; Kampe, S. Microstructural evolution in laser-deposited multilayer Ti-6Al-4V builds: Part I. Microstructural characterization. *Met. Mater. Trans. A* **2004**, *35*, 1861–1867, doi:10.1007/s11661-004-0094-8.
55. Colaço, R.; Vilar, R. Phase selection during laser surface melting of martensitic stainless tool steels. *Scr. Mater*. **1997**, *36*, 199–205, doi:10.1016/s1359-6462(96)00360-0.
56. Hofmeister, W.; Griffith, M. Solidification in direct metal deposition by LENS processing. *JOM* **2001**, *53*, 30–34, doi:10.1007/s11837-001-0066-z.
57. Griffith, M.L. Understanding the microstructure and properties of components fabricated by laser engineered net shaping (LENS™). In Proceedings of the Materials Research Society Symposium, 2000; pp. 625.
58. Grujicic, M.; Cao, G.; Figliola, R. Computer simulations of the evolution of solidification microstructure in the LENS™ rapid fabrication process. *Appl. Surf. Sci*. **2001**, *183*, 43–57, doi:10.1016/s0169-4332(01)00553-0.
59. Ye, R.; Smugeresky, J.E.; Zheng, B.; Zhou, Y.; Lavernia, E.J. Numerical modeling of the thermal behavior during the LENS® process. *Mater. Sci. Eng. A* **2006**, *428*, 47–53, doi:10.1016/j.msea.2006.04.079.
60. Hofmeister, W.; Wert, M.; Smugeresky, J.; Philliber, J.A.; Griffith, M.; Ensz, M. Investigating Solidification with the Laser-Engineered Net Shaping (LENSTM) Process. *JOM* **1999**, *51*, 1–6.
61. Ghosh, S.; Choi, J. Modeling and Experimental Verification of Transient/Residual Stresses and Microstructure Formation in Multi-Layer Laser Aided DMD Process. *J. Heat Transf*. **2005**, *128*, 662–679, doi:10.1115/1.2194037.
62. Yin, H.; Felicelli, S.D. Dendrite growth simulation during solidification in the LENS process. *Acta Mater*. **2010**, *58*, 1455–1465, doi:10.1016/j.actamat.2009.10.053.

63. Flemings, M.C. Solidification processing. *Met. Mater. Trans. A* **1974**, *5*, 2121–2134, doi:10.1007/bf02643923.
64. Aversa, A.; Saboori, A.; Librera, E.; de Chirico, M.; Biamino, S.; Lombardi, M.; Fino, P. The Role of Directed Energy Deposition Atmosphere Mode on the Microstructure and Mechanical Properties of 316L Samples. *Addit. Manuf.* **2020**, 101274, doi:10.1016/j.addma.2020.101274.
65. Song, J.; Deng, Q.; Chen, C.; Hu, D.; Li, Y. Rebuilding of metal components with laser cladding forming. *Appl. Surf. Sci.* **2006**, *252*, 7934–7940, doi:10.1016/j.apsusc.2005.10.025.
66. Syed, W.U.H.; Pinkerton, A.; Li, L. A comparative study of wire feeding and powder feeding in direct diode laser deposition for rapid prototyping. *Appl. Surf. Sci.* **2005**, *247*, 268–276, doi:10.1016/j.apsusc.2005.01.138.
67. Smugeresky, J.; Keicher, D.; Romero, J.; Griffith, M.; Harwell, L. aser engineered net shaping(LENS) process: Optimization of surface finish and microstructural properties. *Adv. Powder Metall. Part. Mater.* **1997**, *3*, 21.
68. Kocabekir, B.; Kaçar, R.; Gündüz, S.; Hayat, F. An effect of heat input, weld atmosphere and weld cooling conditions on the resistance spot weldability of 316L austenitic stainless steel. *J. Mater. Process. Technol.* **2008**, *195*, 327–335, doi:10.1016/j.jmatprotec.2007.05.026.
69. Jacob, G. Prediction of Solidification Phases in Cr-Ni Stainless Steel Alloys Manufactured by Laser Based Powder Bed Fusion Process, NIST. *Adv. Manuf. Ser.* **2018**, *100–114*, 1–38.
70. Guo, P.; Zou, B.; Huang, C.; Gao, H. Study on microstructure, mechanical properties and machinability of efficiently additive manufactured AISI 316L stainless steel by high-power direct laser deposition. *J. Mater. Process. Technol.* **2017**, *240*, 12–22, doi:10.1016/j.jmatprotec.2016.09.005.
71. De Lima, M.S.F.; Sankare, S. Microstructure and mechanical behavior of laser additive manufactured AISI 316 stainless steel stringers. *Mater. Des.* **2014**, *55*, 526–532, doi:10.1016/j.matdes.2013.10.016.
72. Saboori, A.; Toushekhah, M.; Aversa, A.; Lai, M.; Lombardi, M.; Biamino, S.; Fino, P. Critical Features in the Microstructural Analysis of AISI 316L Produced By Metal Additive Manufacturing. *Met. Microstruct. Anal.* **2020**, *9*, 92–96, doi:10.1007/s13632-019-00604-6.
73. Yan, F.; Xiong, W.; Faierson, E.; Olson, G. Characterization of nano-scale oxides in austenitic stainless steel processed by powder bed fusion. *Scr. Mater.* **2018**, *155*, 104–108, doi:10.1016/j.scriptamat.2018.06.011.
74. Babu, S.S.; David, S.A.; Vitek, J.M.; Mundra, K.; Debroy, T. Development of macro- and microstructures of carbon–manganese low alloy steel welds: Inclusion formation. *Mater. Sci. Technol.* **1995**, *11*, 186–199, doi:10.1179/mst.1995.11.2.186.
75. Lou, X.; Andresen, P.L.; Rebak, R.B. Oxide inclusions in laser additive manufactured stainless steel and their effects on impact toughness and stress corrosion cracking behavior. *J. Nucl. Mater.* **2018**, *499*, 182–190, doi:10.1016/j.jnucmat.2017.11.036.
76. Ganesh, P.; Giri, R.; Kaul, R.; Sankar, P.R.; Tiwari, P.; Atulkar, A.; Porwal, R.; Dayal, R.; Kukreja, L. Studies on pitting corrosion and sensitization in laser rapid manufactured specimens of type 316L stainless steel. *Mater. Des.* **2012**, *39*, 509–521, doi:10.1016/j.matdes.2012.03.011.
77. Saboori, A.; Dadkhah, M.; Fino, P.; Pavese, M. An Overview of Metal Matrix Nanocomposites Reinforced with Graphene Nanoplatelets; Mechanical, Electrical and Thermophysical Properties. *Metals* **2018**, *8*, 423, doi:10.3390/met8060423.
78. Saboori, A.; Pavese, M.; Badini, C.; Fino, P. Effect of Sample Preparation on the Microstructural Evaluation of Al–GNPs Nanocomposites. *Met. Microstruct. Anal.* **2017**, *6*, 619–622, doi:10.1007/s13632-017-0397-y.
79. Eo, D.-R.; Park, S.-H.; Cho, J.-W. Inclusion evolution in additive manufactured 316L stainless steel by laser metal deposition process. *Mater. Des.* **2018**, *155*, 212–219, doi:10.1016/j.matdes.2018.06.001.
80. Yadollahi, A.; Shao, S.; Thompson, S.M.; Seely, D.W. Effects of process time interval and heat treatment on the mechanical and microstructural properties of direct laser deposited 316L stainless steel. *Mater. Sci. Eng. A* **2015**, *644*, 171–183, doi:10.1016/j.msea.2015.07.056.
81. Gale, J.; Achuhan, A. Application of ultrasonic peening during DMLS production of 316L stainless steel and its effect on material behavior. *Rapid Prototyp. J.* **2017**, *23*, 1185–1194, doi:10.1108/rpj-09-2016-0140.
82. Saeidi, K.; Gao, X.; Lofaj, F.; Kvetková, L.; Shen, Z. Transformation of austenite to duplex austenite-ferrite assembly in annealed stainless steel 316L consolidated by laser melting. *J. Alloy. Compd.* **2015**, *633*, 463–469, doi:10.1016/j.jallcom.2015.01.249.
83. Zhang, K.; Wang, S.; Liu, W.; Shang, X. Characterization of stainless steel parts by Laser Metal Deposition Shaping. *Mater. Des.* **2014**, *55*, 104–119, doi:10.1016/j.matdes.2013.09.006.
84. Yang, N.; Yee, J.; Zheng, B.; Gaiser, K.; Reynolds, T.; Clemon, L.; Lu, W.Y.; Schoenung, J.M.; Lavernia, E.J. Process-Structure-Property Relationships for 316L Stainless Steel Fabricated by Additive Manufacturing

and Its Implication for Component Engineering. *J. Spray Technol.* **2016**, *26*, 610–626, doi:10.1007/s11666-016-0480-y.

85. Saeidi, K.; Gao, X.; Zhong, Y.; Shen, Z. Hardened austenite steel with columnar sub-grain structure formed by laser melting. *Mater. Sci. Eng. A* **2015**, *625*, 221–229, doi:10.1016/j.msea.2014.12.018.
86. Kim, N.-K.; Woo, W.; Kim, E.-Y.; Choi, S.-H. Microstructure and mechanical characteristics of multi-layered materials composed of 316L stainless steel and ferritic steel produced by direct energy deposition. *J. Alloy. Compd*. **2019**, *774*, 896–907, doi:10.1016/j.jallcom.2018.09.390.
87. Park, J.S.; Park, J.H.; Lee, M.-G.; Sung, J.H.; Cha, K.J.; Kim, D.H. Effect of Energy Input on the Characteristic of AISI H13 and D2 Tool Steels Deposited by a Directed Energy Deposition Process. *Met. Mater. Trans. A* **2016**, *47*, 2529–2535, doi:10.1007/s11661-016-3427-5.
88. Gülenç, B.; Develi, K.; Kahraman, N.; Durgutlu, A. Experimental study of the effect of hydrogen in argon as a shielding gas in MIG welding of austenitic stainless steel. *Int. J. Hydrog. Energy* **2005**, *30*, 1475–1481, doi:10.1016/j.ijhydene.2004.12.012.
89. Boes, J.; Röttger, A.; Becker, L.; Theisen, W. Processing of gas-nitrided AISI 316L steel powder by laser powder bed fusion—Microstructure and properties. *Addit. Manuf.* **2019**, *30*, 100836, doi:10.1016/j.addma.2019.100836.
90. Morrow, B.; Lienert, T.J.; Knapp, C.M.; Sutton, J.O.; Brand, M.J.; Pacheco, R.M.; Livescu, V.; Carpenter, J.S.; Gray, G.T. Impact of Defects in Powder Feedstock Materials on Microstructure of 304L and 316L Stainless Steel Produced by Additive Manufacturing. *Met. Mater. Trans. A* **2018**, *49*, 3637–3650, doi:10.1007/s11661-018-4661-9.
91. Ganesh, P.; Kaul, R.; Sasikala, G.; Kumar, H.; Venugopal, S.; Tiwari, P.; Rai, S.; Prasad, R.C.; Kukreja, L.M. Fatigue Crack Propagation and Fracture Toughness of Laser Rapid Manufactured Structures of AISI 316L Stainless Steel. *Met. Microstruct. Anal.* **2014**, *3*, 36–45, doi:10.1007/s13632-013-0115-3.
92. Gordon, J.; Hochhalter, J.; Haden, C.; Harlow, D.G. Enhancement in fatigue performance of metastable austenitic stainless steel through directed energy deposition additive manufacturing. *Mater. Des*. **2019**, *168*, 107630, doi:10.1016/j.matdes.2019.107630.